

A spin-1 representation for dual-funnel energy landscapes

Justin E. Elenewski, Kirill A. Velizhanin, and Michael Zwolak

Citation: *The Journal of Chemical Physics* **149**, 035101 (2018); doi: 10.1063/1.5036677

View online: <https://doi.org/10.1063/1.5036677>

View Table of Contents: <http://aip.scitation.org/toc/jcp/149/3>

Published by the *American Institute of Physics*

PHYSICS TODAY

WHITEPAPERS

ADVANCED LIGHT CURE ADHESIVES

Take a closer look at what these environmentally friendly adhesive systems can do

READ NOW

PRESENTED BY
 **MASTERBOND**
ADHESIVES | SEALANTS | COATINGS

A spin-1 representation for dual-funnel energy landscapes

Justin E. Elenewski,^{1,2} Kirill A. Velizhanin,³ and Michael Zwolak^{1,a)}

¹Center for Nanoscale Science and Technology, National Institute of Standards and Technology, Gaithersburg, Maryland 20899, USA

²Maryland Nanocenter, University of Maryland, College Park, Maryland 20742, USA

³Theoretical Division, Los Alamos National Laboratory, Los Alamos, New Mexico 87545, USA

(Received 17 April 2018; accepted 1 July 2018; published online 20 July 2018)

The interconversion between the left- and right-handed helical folds of a polypeptide defines a dual-funneled free energy landscape. In this context, the funnel minima are connected through a continuum of unfolded conformations, evocative of the classical helix-coil transition. Physical intuition and recent conjectures suggest that this landscape can be mapped by assigning a left- or right-handed helical state to each residue. We explore this possibility using all-atom replica exchange molecular dynamics and an Ising-like model, demonstrating that the energy landscape architecture is at odds with a two-state picture. A three-state model—left, right, and unstructured—can account for most key intermediates during chiral interconversion. Competing folds and excited conformational states still impose limitations on the scope of this approach. However, the improvement is stark: Moving from a two-state to a three-state model decreases the fit error from $1.6 k_B T$ to $0.3 k_B T$ along the left-to-right interconversion pathway. *Published by AIP Publishing.* <https://doi.org/10.1063/1.5036677>

I. INTRODUCTION

While most biomolecular helices possess a right-handed orientation, a small minority are predisposed to assume a left-handed fold.¹ This chiral propensity may be enhanced through the introduction of achiral amino acids, such as 2-aminoisobutyric acid (Aib)—noted for its ability to induce a prominent left-handed helical population in biomimetic peptides (Fig. 1).² While useful as a probe of biological organization, this observation also constitutes a general rule: a helix-forming polymer will demonstrate a preferred axial chirality when it is constructed from chiral blocks. By contrast, polymers derived from achiral blocks exhibit a degeneracy of left-handed (*L*) and right-handed (*R*) helical folds, forming an effective two-state system.³ Deviations from this behavior must be associated with induced chirality, either from the solvent environment or from chiral structural elements flanking the polymer.

This tunable two-state character has been exploited in the design of foldamer-based nanodevices.^{4–6} By introducing structural features that extend beyond standard biological motifs, these materials can be engineered to include distinctive photoreactive,⁷ thermoresponsive,^{8,9} pore-forming,¹⁰ and ligand binding functionalities.^{11,12} Aib-containing decamers, in particular, form stable helices and have found use as actuators within biomimetic receptors,^{6,13,14} and photoswitches.⁷ In this case, triggering a conformational shift in the N-terminal sensor domain—through either ligand binding or photoexcitation—presumably biases the free energy landscape toward the opposite helical chirality, analogous to solvent-driven transitions in polyproline peptides.^{15,16} This shift results in an $L \leftrightarrow R$

interconversion, the subsequent structural reorganization of a covalently linked C-terminal reporter, and the ultimate detection of an activation signal. While promising as biomimetic devices, these systems also afford a fundamental opportunity to explore the translation of local molecular interactions into folding and function, outside the confines of natural biological systems.¹⁷

The static and dynamic properties of a macromolecule are dictated by the architecture of its potential energy landscape.^{18–20} In the case of biomolecules, these landscapes are minimally frustrated, containing the smallest possible set of competing low-energy conformations, separated by high potential barriers. This principle often affords a sharply funneled profile, with the so-called native state lying at the global minimum and successive “excited” states occupying higher-lying local minima. These minima collectively define the stable conformers of the molecule, while barriers in the landscape dictate the kinetic profile for conformational transitions.

Multifunctional biomolecules deviate from this paradigm, delivering a potential energy landscape that contains separate funnels for each functional conformer.²¹ This organizational principle extends to helical foldamers, where left- and right-handed orientations correspond to separate funnel minima in a dual-funnel energy landscape.^{22,23} While increasingly recognized in a biological context, the initial theoretical foundation for these systems was derived to describe dual-funnel solid-solid transitions of small Lennard–Jones (LJ) clusters.^{24,25} These investigations delivered fundamental insight into the hallmarks of multifunnel landscapes and illustrated how landscape features can mediate processes that range from kinetic trapping to phase changes in extremely finite systems. Explorations of cluster landscapes have likewise inspired, and serve as a benchmark for, ergodic sampling methods in molecular

^{a)}Electronic mail: mpz@nist.gov

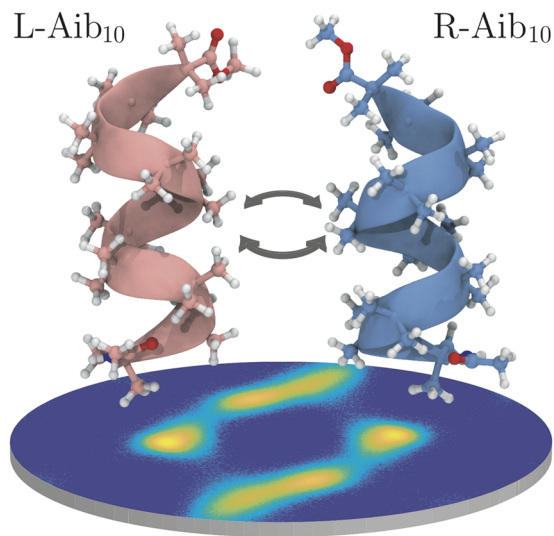


FIG. 1. Interconversion between left- and right-handed helical conformations in an Aib₁₀ peptide foldamer.

simulations,^{26–34} global optimization schemes,³⁵ and path-sampling frameworks for rare-event dynamics.^{36–40} These computational advances have, in turn, facilitated more recent studies of biological and biomimetic systems, including those undergoing helix chirality inversions^{15,22,23,41} and containing bistable switching motifs.^{42–44}

While certain biomolecules have been well explored, a systematic theory-guided approach to the foldamer design is impeded by the complex nature of multifunnel energy landscapes. In principle, these may only be mapped using costly numerical simulations.^{44,45} Nonetheless, a suitable analytical model—parameterized using discrete calculations at the single-block level—might dramatically accelerate these efforts while retaining acceptable quantitative accuracy. Numerous computational techniques have been applied to Aib-containing helices in order to understand the form that such a model should take.^{46–53} Nonetheless, the majority of these are limited in their sampling of conformational dynamics during the $L \leftrightarrow R$ transition. Motivated by the studies of energy transport in the Aib₉ peptide foldamer,^{54–58} more recent efforts have applied long-time scale molecular dynamics simulations, Markov state modeling, and principal component analysis (PCA) to these systems.^{59,60} The resulting data suggest that Aib₉ has a conformational landscape where long time scale (ns to μ s) dynamics are ultimately slaved to short time scale (ps) hydrogen bonding transitions through a hierarchy of time scales—a feature characteristic of systems with a multi-funnel architecture.^{61–63} A coarse-grained energy landscape was proposed, parameterized in terms of backbone dihedral angles (ϕ , ψ), with conformational substates determined by discrete per-residue changes in helical chirality. In this manner, each residue is assigned to either a left (L) or right (R) conformational substate, though the authors did not make this statement quantitative.^{59,60} While more elaborate coarse-grained models can capture the dynamics of helix chirality inversion,²³ it is unclear if this minimal description can do the same.

To explore this physically intuitive proposal and assess the limits of coarse-graining, we have constructed an explicit

representation of the L/R -model using an Ising-like Hamiltonian. Large-scale replica-exchange molecular dynamics (REMD) simulations and an unsupervised clustering approach were employed for parameterization, affording a granular picture of the potential energy landscape. Our observations indicate that a two-state representation is insufficient to describe the structural diversity inherent in the $L \leftrightarrow R$ transition. A three-state spin-1 model yields better performance by explicitly including unstructured regions. However, the model still exhibits systematic deviations from all-atom simulations. These inconsistencies arise from numerous factors, including the presence of “excited” conformational substates and the existence of distinct competing helical folds. Taken together, our observations provide a minimal bound on the complexity of analytical models that accurately describe simple foldamers such as Aib _{N} , where N is the number of repeats, and attest to the necessity of explicit simulation in characterizing these systems.

II. THEORY AND METHODS

A. Spin models

We consider an unbranched foldamer containing N linearly ordered blocks. In the simplest case, each of these blocks might be classified as either a left-handed (L) or right-handed (R) configuration according to its backbone dihedral angles (the Appendix). An energetic gain of $J < 0$ per site is expected when consecutive blocks share the same helical orientation ($\dots RR \dots$ or $\dots LL \dots$)—promoting the formation of homochiral domains—and an energetic penalty of $-J > 0$ encountered at a domain wall between left- and right-helical regions ($\dots LR \dots$ or $\dots RL \dots$). The simplest Hamiltonian that describes these interactions is a *classical* “ferromagnetic” spin-1/2 Ising model,

$$E_{\mathcal{I}} = \sum_{\alpha=1}^{N-1} \hat{J}(\sigma_{\alpha+1}, \sigma_{\alpha}), \quad (1)$$

where the spin $\sigma_{\alpha} \in \{L, R\}$ residing on block α is assigned to either a right-handed (R) or left-handed (L) configuration. The spin-spin coupling matrix \hat{J} is symmetric, and all elements are of the same magnitude, $J = \hat{J}(R, R) = \hat{J}(L, L) = -\hat{J}(L, R) = -\hat{J}(R, L)$. The [supplementary material](#) shows the effect of asymmetric couplings and discusses our approach to fitting (Sec. I A and Figs. S1–S5 of the [supplementary material](#)). We will discuss the difficulties encountered with this simple approach.

The energy, Eq. (1), can be extended to a spin-1 scenario, where an unstructured random coil state U exists alongside the L and R configurations ($\sigma_{\alpha} \in \{L, U, R\}$). We take the coil state to always refer to the unstructured polymer or region. For simplicity, we assume that the extended coil stretches have no inter-site coupling $\hat{J}(U, U) = 0$, nor do they make an energetic contribution when contacting helical regions $\hat{J}(L/R, U) = 0$ (Sec. I B, Figs. S6 and S7 of the [supplementary material](#)). This construction differs from Zimm–Bragg⁶⁴ and Lifson–Roig⁶⁵ models for the helix-coil transition, where an additional statistical weight for nucleation is assigned to helix termini that flank unfolded regions. The inclusion of a nucleation penalty

$\hat{J}(L/R, U) \neq 0$, or a correction for flexible helix termini, has only a modest impact on our model (see Figs. S7 and S8 of the [supplementary material](#)).

The persistence of extended coils will depend on a variety of factors, including the interaction of side chain and backbone atoms with the encapsulating solvent. This effect may be captured through an on-site solvation energy K_S that is associated with unstructured peptide regions. We may also define a contribution $\hat{K}(L/U/R)$ that reflects the tendency of a given conformation to reside in rotameric minima (not including cooperative factors, such as hydrogen bonding), leading to an on-site Hamiltonian term

$$E_{\mathcal{O}} = \sum_{\alpha=1}^N \hat{K}(\sigma_{\alpha}). \quad (2)$$

In practice, it is convenient to set $\hat{K}(L) = \hat{K}(R) = 0$ and introduce a single nonzero on-site parameter $\hat{K}(U) = K_S - K_0$ that reflects the impact of solvation (and other factors that impact the “on site” energy of a block) on the extended coil state (see Figs. S9 and S10 of the [supplementary material](#)). Under these considerations, $\hat{K}(U) < 0$ promotes and $\hat{K}(U) > 0$ penalizes the formation of extended coil regions. For Aib peptides in chloroform, one would expect a $\hat{K}(U) > 0$ as contacts between the polar backbone amides and the nonpolar solvent would be disfavored.

In a realistic foldamer, coiled regions will admit a multitude of conformations, while the comparatively rigid helical residues are likely to cluster around a single conformational state. This behavior may be accommodated by introducing the contribution of rotameric entropy to the free energy of the system,

$$S_{\mathcal{R}} = k_B \sum_{i \in \mathcal{C}} (n_i - 1) \cdot s, \quad (3)$$

where n_i is the length of the i -th coiled stretch, $k_B \cdot s$ is a unit of conformational (rotameric) entropy, and k_B is the Boltzmann constant. The summation runs over indices in the set of coiled regions, \mathcal{C} , defined as a repeat of two or more consecutive U sites in a given peptide conformation. The high flexibility of helix termini, coupled with their ambiguous dihedral assignments, necessitates their exclusion when determining membership in \mathcal{C} . The appearance of $(n_i - 1)$ in Eq. (3) and the definition of \mathcal{C} both require an explanation. While a single U site results in a kinked helix—and a slight increase in entropy—broad conformational (rotameric) sampling only occurs when there is junction between two U sites (an upper bound for the kink entropy is given by Fig. S11b of the [supplementary material](#); however the minute conformational variability observed in all-atom MD is beyond the scope of our model). As a consequence of this, an expression scaling as n_i results in an overestimation of the entropy for otherwise structured states, leading to the use of an $(n_i - 1)$ term (see Fig. S11 of the [supplementary material](#)).

These considerations collectively define the relevant contributions to the Gibbs free energy for a solvated helical foldamer, containing both helical and unfolded segments,

$$G_C = E_{\mathcal{O}} + E_{\mathcal{I}} - TS_{\mathcal{R}} + pV. \quad (4)$$

As a matter of convention, the free energy of the j -th spin configuration $\Delta G_{C,j} = G_{C,j} - G_{C,0}$ will be measured relative to the absolute free energy $G_{C,0}$ of the lowest energy spin configuration(s) in a given ensemble. The Hamiltonian components of this model are exactly solvable, and the partition function may be evaluated using transfer matrix techniques. Equation (4) includes a contribution from volume, pV , where p (V) is the pressure (volume), that is necessary for completeness. We may alternatively drop this explicit dependence, effectively wrapping this parameter into other terms appearing in Eq. (4) by fitting simulation data. This will be addressed later.

B. All-atom simulations

Molecular dynamics simulations were performed using a ten residue stretch (Aib₁₀) of 2-aminoisobutyric acid, with initial backbone dihedrals assigned from the Dunbrack rotamer library for a right-handed 3_{10} helix.⁶⁶ The model was embedded in a (5 nm)³ cubic cell, containing 922 chloroform molecules, and packed to the density of the bulk solvent.⁶⁷ C- and N-termini were methylated and acetylated, respectively, and simulation physics is described using the CHARMM36 force field⁶⁸ and the LAMMPS package.⁶⁹ CHARMM cross term map (CMAP) corrections were not employed.⁷⁰ While this modification has been demonstrated to improve α -helix folding cooperativity,^{68,71} it dramatically overestimates the α -helical character for model helices.⁷² Since Aib₁₀ is characterized by the nontrivial 3_{10} -helical content, this would have questionable transferability without major reparameterization.

Lennard–Jones and Coulomb interactions were computed using conventional CHARMM pair potentials, conjoined with an additional electrostatic damping term to maintain compatibility with particle–particle–particle mesh summation (force cutoff = 6.95×10^{-3} pN). Switching functions were employed to rescale coupling between atomic pairs separated by more than 1.0 nm, with the interatomic potential vanishing beyond 1.35 nm separation. A time step of 1.0 fs was used for all calculations within a scheme⁷³ that employs a velocity Verlet integrator, modified Nosé–Hoover thermostat, and Martyna–Tobias–Klein barostat,⁷⁴ alongside a Parrinello–Rahman representation⁷⁵ for the strain energy, allowing us to reproduce the correct probability distribution for the isobaric–isothermal (NPT) ensemble. The damping period of the thermostat was set to 100 fs, while the damping period of the barostat was set to 1000 fs and coupled to a chain of eight members. Isotropic cell fluctuations were allowed in all directions, and initial velocities were assigned according to Gaussian distributions for both linear and angular momenta at a given temperature.

The Aib₁₀ model was subjected to an initial 22 ns NPT equilibration, providing a starting point for subsequent replica exchange simulations. REMD runs were performed using 48 replicas in an NPT scheme,^{76,77} with temperatures spanning between $T_i = 230$ K and $T_f = 465$ K. Exchanges were attempted every 500 fs, yielding an acceptance ratio of 32% for all simulations. REMD simulations were equilibrated for further 150 ns, followed by a 500 ns production run. Conformational clusters were determined using a running k -means scheme and

a metric based on the root-mean-square deviation (RMSD) of heavy backbone atoms (0.26 nm, cutoff radius). This procedure is sufficient to converge the energies of ground-state clusters—presumed to be degenerate at all temperatures—to within a deviation of $0.07 k_B T$ when sampling below 300 K. The persistence of this criterion for over 50 ns of sampling was taken as a hallmark for convergence, as force field deficiencies may prevent complete degeneracy from occurring on an accessible time scale during our simulations.⁵⁹

III. RESULTS AND DISCUSSION

A. Aib₁₀ energy landscape

The conformational dynamics of Aib-based polypeptides have been experimentally characterized in a spectrum of solvents. However, their behavior in chloroform has a particularly distinguished history. Under these conditions, it has been proposed that a glass-like dynamical transition occurs in Aib-Ala-(Aib)₆ derivatives,^{54–57,78} as reflected through temperature-dependent energy transport, though the nature of this transition—and the changes in energy transport—remains contentious, even among the same group of authors.^{58,59,79,80} More concretely, a nonpolar environment mimics the artificial membranes in which many foldamer-based molecular sensors are intended to operate.^{7,14} These factors—combined with the absence of solvent hydrogen bonding or complex electrostatics—motivated us to adopt this model system.

An enhanced-sampling approach was employed to facilitate the exploration of conformational space, using all-atom REMD simulations to sample the NPT ensemble for an explicitly solvated Aib₁₀ peptide. This protocol generates approximately 10^6 conformers for each temperature; however, the construction of an energy landscape requires either projection onto a lower-dimensional subspace or the reductive classification of these peptide conformations into a smaller set of states. We adopted the latter approach—a granular quantification of minor intermediates along the transition pathway. While a full-dimensional approach might involve the use of disconnectivity graphs and related classification methods, a simple clustering scheme is sufficient for our purposes.²⁴ This character may be obscured when using PCA-based methods. Classification was accomplished using a k -means clustering scheme, in which a given trajectory frame is assigned to a cluster only if the running intra-cluster RMSD is less than 0.26 nm from the cluster centroid. For a 500 ns REMD trajectory, this affords clusters containing ≈ 400 states at each temperature that is sampled between 230 K and 330 K. With this classification in hand, a relative free energy

$$\Delta G_{jk} = -k_B T \log [P_k/P_j] \quad (5)$$

may be calculated between states of populations P_j and P_k , respectively. For simplicity, we assume that free energies are measured with respect to the most populous cluster in each ensemble, allowing ΔG_j to be indexed by a single parameter.

REMD simulations reveal an energy landscape that contains two distinct folding funnels, corresponding to left- and right-handed conformations of the peptide helix (Fig. 2). The

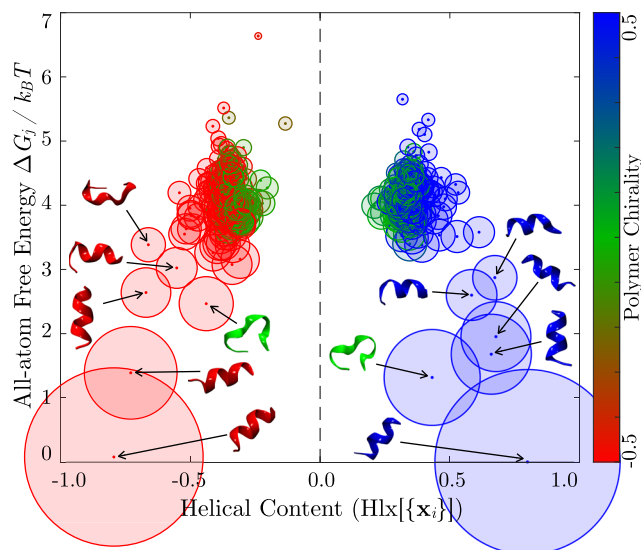


FIG. 2. Free energy landscape of Aib₁₀ at $T = 300$ K. Each data point represents one of $N = 433$ clusters, and the size of each point is scaled relative to the number of states contained within the respective cluster.

native helical states in each funnel are nearly isoenergetic; however, a degree of asymmetry exists in distribution of clusters. This is likely a collective effect, resulting from clustering artifacts, initial conditions, sampling limitations, and a degree of bias induced by the terminal patches that maintain electrostatic neutrality. Interestingly, (a more sizable) asymmetry was observed in a previously reported map of the Aib landscape derived following long-time scale MD simulations and dimensional reduction of the data.⁵⁹ On a separate note, the gap in helical content between left- and right-handed funnels is intrinsic to the function $\text{Hlx}[\{\mathbf{x}_i\}]$ (see the Appendix), which accounts for oriented twists in the peptide backbone, reflecting an ‘intrinsic helical content’ associated with the gyration of the peptide chain.

While the precise cluster assignments in each funnel are not identical, the overall distribution of these states remains quite similar. Both funnels are dominated by highly populated clusters of helix-rich states at low energies, expanding into a large set of high-entropy states with a low helical content at higher energies. This high energy region also contains ‘excited’ helical states, in which an energetically unfavorable conformation is assumed while preserving the overall helical fold. An apparent crossing between funnels, where the fold becomes largely unstructured, occurs around $T = 4 k_B T$ consistent with prior PCA-based landscapes.^{59,60} This system is distinguished from other foldamers by the achiral nature of Aib, affording a highly symmetric and degenerate energy landscape. By contrast, helices that are derived from chiral blocks^{15,22,23} often demonstrate some degree of energetic asymmetry, while clusters such as LJ₃₈ possess energetically asymmetric basins with markedly different topographies.²⁵

The low energy clusters in this ensemble are primarily α -helical, transitioning to a combination of unfolded and 3₁₀-character with increasing energy (Fig. 3). At first glance, this appears to contradict experiment, as crystallography,^{81–83} optical,^{84–86} and magnetic resonance spectroscopies suggest

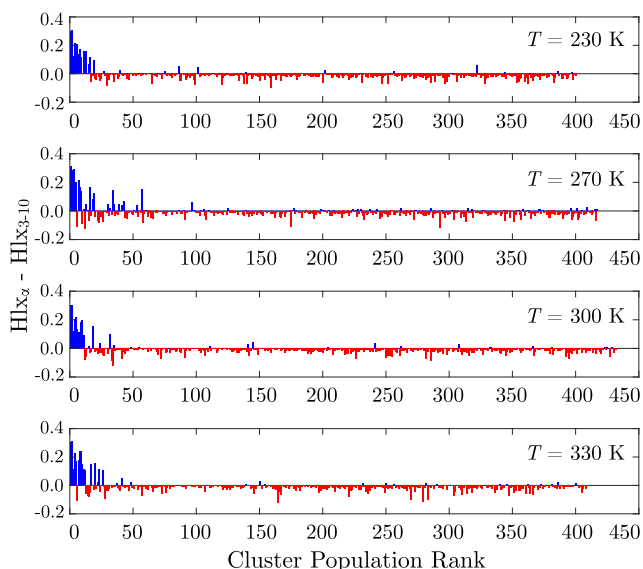


FIG. 3. Temperature-dependent helical content within the Aib₁₀ landscape, demonstrating an excess of either α -helical (blue) or 3_{10} -helical (red) character. Clusters are ranked in the order of decreasing population (i.e., increasing free energy).

that short (≤ 7 residues) Aib peptides exist as 3_{10} -helices in weakly dielectric environments. This picture is nuanced, as both α - and 3_{10} -conformations—with a dominant α -helical population—have been observed in polar and moderately polar solvents (water, dimethyl sulfoxide / DMSO).^{48,87–89} Taken together, these data indicate that Aib conformations exhibit a high degree of environmental sensitivity, with 3_{10} -helical content predominating for short helices in nonpolar media and at higher temperatures.⁹⁰ Since our ten-residue model is longer than the peptides employed in most experimental efforts, it is plausible that a greater degree of α -helical content may occur in this system, with the early stages of folding templated by a 3_{10} -helix.⁹¹ This behavior is consistent with MD simulations using a custom AMBER-based force field for Aib^{52,53} and long-time scale trajectories of Aib₉ dynamics using GRO-MOS96, which reveal an increasing proportion of α -helical character for longer chains.⁵⁹ Nonetheless, the dominant helical fold, and any force-field dependence, will not markedly alter our conclusions. The key observation herein is the coexistence of two distinct helical populations with different physical characteristics.

The state distribution within the Aib₁₀ landscape is readily analyzed using the density of conformational cluster states $\rho(E)$ that are observed at each replica temperature,

$$\rho(E) = \sum_{j=1}^{N_C} P_j e^{-(E-\Delta G_j)^2/2\sigma^2}, \quad (6)$$

where N_C is the number of k -means clusters calculated for a given replica, P_j is the population of the j -th cluster, ΔG_j is the free energy of the j -th cluster, and σ^2 accounts for the inter-cluster conformational variance (Fig. 4). These data exhibit a weak temperature dependence, characterized by a 5% increase in the number of conformers lying below $4 k_B T$ as the temperature is increased from 230 K to 330 K. Notably, these data do not demonstrate any obvious signatures of a transition between 250 K and 270 K, where prior experiments and simulations

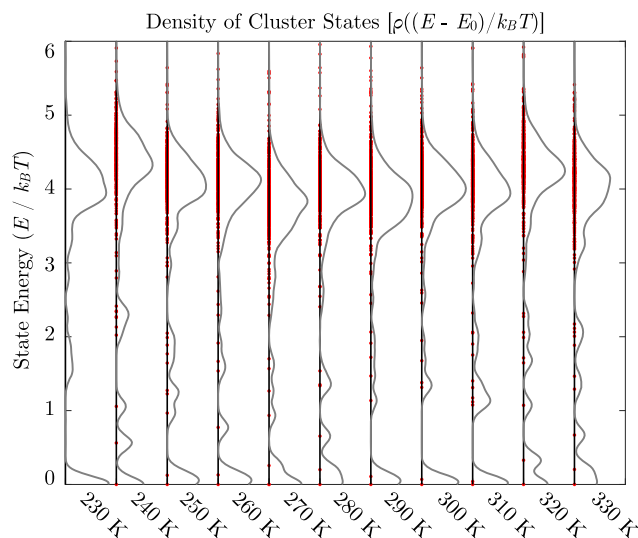


FIG. 4. Density of conformational clusters, populated according to the number of members in each cluster, for all-atom replica exchange simulations with base temperatures spanning between 220 K and 330 K. The density of states was calculated using $\sigma^2 = 0.01$ as a smearing parameter.

have suggested that the Aib might undergo a protein dynamical transition.^{54–56,58,59,79,80} A dynamical transition cannot be excluded without a more comprehensive analysis, as these inherently coarse-grained clusters may obscure subtle changes associated with this phenomenon. Furthermore, a dynamical transition is canonically associated with a redistribution of barrier heights in the energy landscape, which is not determined in this work. These effects are expected, at most, to modestly perturb the landscape minima.

B. Spin representations of the energy landscape

The energy landscape of Aib₁₀—parameterized by the backbone dihedrals—reflects the secondary structure of conformational substates and bounds the complexity of coarse-grained models. The free energy surface corresponding to a single Aib residue, $\Delta G_1(\phi, \psi)$, is foundational to this classification. When calculated from the REMD ensemble at $T = 300$ K, this surface contains four primary minima, including left-handed ($\phi \approx -50^\circ, \psi \approx -55^\circ$) and right-handed ($\phi \approx 50^\circ, \psi \approx 55^\circ$) helical regions alongside a pair of broad-shouldered basins (right-handed: $\phi \approx -65^\circ, \psi \approx 55^\circ$; left-handed: $\phi \approx 65^\circ, \psi \approx -55^\circ$) that define extended conformations [Fig. 5(a), Fig. S9 of the [supplementary material](#)]. REMD simulations reveal a distribution of minima and interconversion barriers (ranging between $4k_B T$ and $5k_B T$) that resemble earlier simulations of Aib dynamics, suggesting that our computational approach captures the general condensed phase behavior of Aib.^{52,59}

In a similar manner, it is straightforward to derive a free energy surface $\Delta G_{10}(\vec{\phi}, \vec{\psi})$ for entire Aib₁₀ peptides in terms of the mean backbone dihedrals $\vec{\phi}_j = (N-2)^{-1} \sum_{\alpha=2}^{N-1} \phi_{j,\alpha}$ and $\vec{\psi}_j = (N-2)^{-1} \sum_{\alpha=2}^{N-1} \psi_{j,\alpha}$, where the index α runs over residues within the j -th Aib₁₀ configuration. Summation is restricted to interior residues as the highly flexible terminal sites can only be assigned a single dihedral parameter. The resulting landscape is more complex than that of a single Aib residue, containing helical substates that are connected by a near-continuum

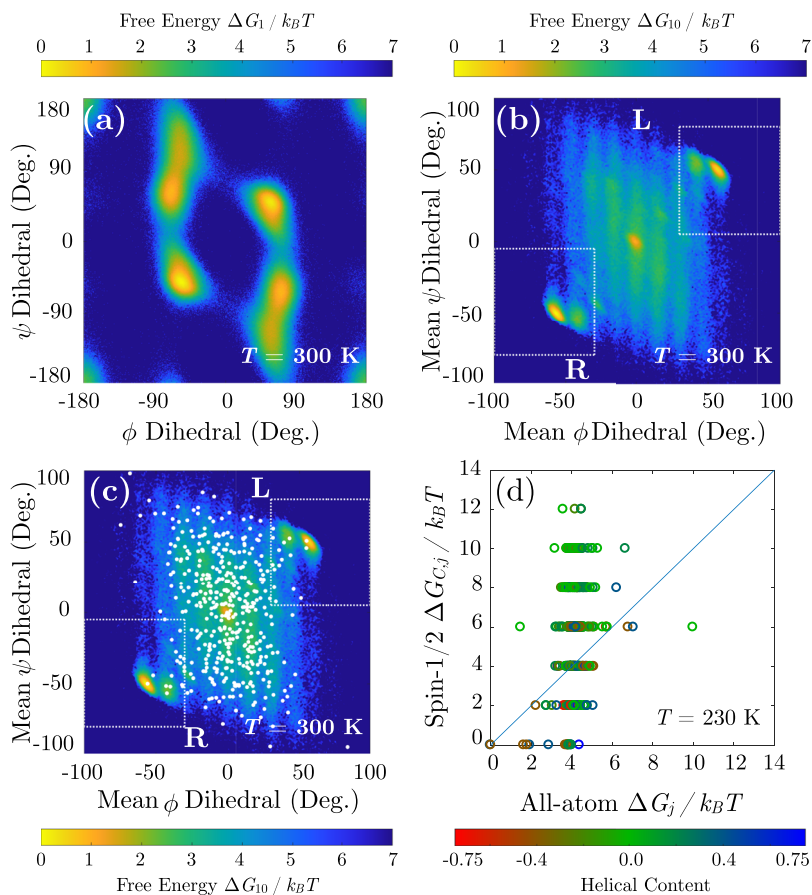


FIG. 5. Quantification of the Aib₁₀ energy landscape: (a) free energy landscape $\Delta G_1(\phi, \psi)$ assumed by Aib when incorporated into Aib₁₀, derived from the REMD distribution of (ϕ_j, ψ_j) backbone dihedral angles; (b) free energy surface $\Delta G_{10}(\bar{\phi}, \bar{\psi})$ for individual Aib₁₀ conformers calculated from a distribution of the average backbone dihedrals $(\bar{\phi}_j, \bar{\psi}_j)$; (c) overlay of k -means centroids (white dots) with the $\Delta G_{10}(\bar{\phi}, \bar{\psi})$ landscape; and (d) cross correlation between the j -th cluster energy, ΔG_j determined from REMD simulations, and the j -th centroid energy $\Delta G_{C,j}$ calculated using the spin-1/2 Hamiltonian $\Delta G_C = \Delta E_{\mathcal{T}}$ with unit coupling ($\hat{J}(R, R) = -1.0 k_B T$; $\hat{J}(L, R) = 1.0$). The root mean square error (RMSE) between ΔG_j and $\Delta G_{C,j}$ is $2.8 k_B T$; however this is biased toward unstructured states; the RMSE for states lying along the helix-coil transition (Fig. 6) is $1.6 k_B T$. Energy landscapes were determined using 10^6 Aib₁₀ conformers, extracted from REMD simulations at $T = 230$ K. Boxed areas in (b) and (c) denote the preferred subregions of dihedral space for left- and right-handed helices.

of weakly structured intermediate configurations [Fig. 5(b)]. This architecture is well mapped by k -means clusters, with centroids that are both localized in the minima of $\Delta G_{10}(\bar{\phi}, \bar{\psi})$ and diffusely distributed throughout the interstitial parameter space [Fig. 5(c)].

While this energy profile is consistent with earlier simulations, the preceding efforts identified fewer states within in the energy landscape.⁵⁹ This deviation is likely associated with the PCA-based dimensional reduction employed by other authors. In this case, PCA component vectors were shown to convolve the ϕ and ψ backbone dihedrals with undetermined lower-weight parameters. The resulting landscape corresponds (approximately) to a configuration in which conformations from our k -means clusters are averaged according to their backbone dihedrals within overlapping neighborhoods (c.f. Fig. 5). This redistribution and averaging affords a smoothed map of conformational space, while impeding the detection of nuanced details that are captured by our clustering. In a similar manner, the landscape given by ΔG_{10} contains numerous minima that are better differentiated by the geometric (ϕ, ψ) backbone dihedrals than the admixed parameters resulting from PCA. The marginalization of fine landscape features with certain order parameters is a well-known complication of dimensional reduction^{34,92–94} though any given pair of these parameters may be related through a well-defined scaling transformation.⁹⁴

The Aib₁₀ landscape contains numerous conformations (70.8% of the ensemble) that lie outside the basins dominated by the left- and right-handed helical character (Fig. 5 and Fig.

S9 of the [supplementary material](#)). At first glance, this would appear to preclude a two state model, even when restricted to core regions of the Aib helix. To test this assumption, the centroids at $T = 230$ K were given a binary classification by setting $\sigma_\alpha = R$ when $\psi_\alpha \leq -\phi_\alpha$ and $\sigma_\alpha = L$ when $\psi_\alpha \geq -\phi_\alpha$, following an earlier proposal.⁵⁹ Using this ensemble, the centroid energies calculated using the spin-1/2 Hamiltonian $\Delta G_{C,j} = \Delta E_{\mathcal{T}}$ exhibit extremely weak correlation (particularly for structured conformers) with the energies ΔG_j derived from the REMD landscape, indicating that unstructured configurations are critical to constructing a simplified model of Aib₁₀ dynamics. This observation is underscored by theoretical investigations of other bistable helical foldamers, which note the importance of unstructured states to either primary or secondary pathways for helix chirality inversion.^{15,22,41}

A more meaningful classification scheme becomes apparent when introducing an unfolded coil (U) configuration, leading to a three-state spin-1 representation of the energy landscape. To implement this approach, every cluster centroid may be encoded as a spin configuration between residues i and $i + 1$ using the function $\text{hcx}\{\{\mathbf{x}_i\}, \{\mathbf{x}_{i+1}\}\}$ [Eq. (A5)]. These data may then be employed to compute the energy $\Delta G_{C,j}$ of the j -th centroid and compared directly to with the corresponding cluster energy ΔG_j from the all-atom replica ensemble.

The simplest three-state model for Aib₁₀ employs only the spin-spin Hamiltonian term $\Delta G_C = \Delta E_{\mathcal{T}}$ to quantify interactions between structural motifs. This model demonstrates modest agreement with the REMD cluster distribution at low

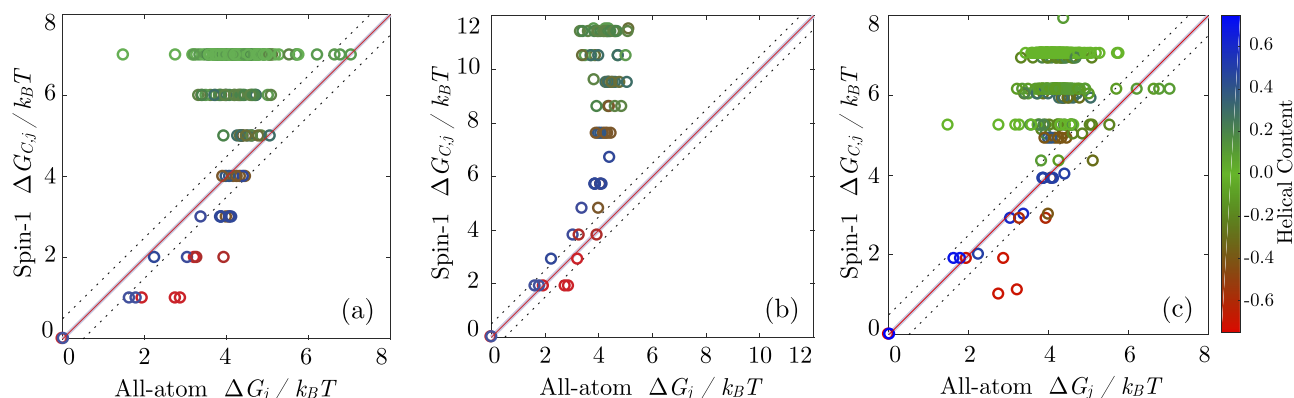


FIG. 6. Cross correlation between the j -th cluster energy, ΔG_j determined from REMD simulations at $T = 230$ K, and the j -th centroid energy $\Delta G_{C,j}$ calculated using spin-1 Hamiltonians. Configurations correspond to (a) $\Delta G_C = \Delta E_T$, (b) $\Delta G_C = \Delta E_T + \Delta E_O$, and (c) $\Delta G_C = \Delta E_T + \Delta E_O - T\Delta S$. Points are colored according to their helical content, spanning from right-handed helices (blue) to random coil (green) to left-handed helices (red) [parameters are determined by setting $\hat{J}(L, L) = \hat{J}(R, R) = -1.0 k_B T$ and $\hat{J}(L, R) = 1.0 k_B T$ (see Sec. I of the [supplementary material](#)) and employing a systematic fitting procedure to find $K_U = 0.9 k_B T$, $s = 0.9$]. Dashed lines denote a range within $\pm 0.5 k_B T$ of the diagonal. Fitting was performed by maximizing the number of clusters ($N_{\text{fit}} = 26$) for which $|\Delta G_{C,j} - \Delta G_j| \leq 0.5 k_B T$ and simultaneously minimizing $|\Delta G_{C,j} - \Delta G_j|$, affording an RMSE of $0.3 k_B T$ for fitting points (overall RMSE = $2.4 k_B T$). This corresponds to 15% of the spin-1/2 RMSE for clusters lying along the helix-coil transition [Fig. 5(d)]. We note that the solvent and entropic terms are both physically tied to the three-state model, as they reflect the behavior of the unstructured state. Therefore, they are not included in the spin-1/2 model of Fig. 5(d).

energies; however, a pronounced deviation is observed for high-entropy states in which random coil character is dominant [Fig. 6(a)]. The inclusion of a correction $\Delta G_C = \Delta E_T + \Delta E_O$ that disfavors solvent-exposed coils strengthens this correspondence for a number of clusters in the well-folded region ($\Delta G_j, \Delta G_{C,j} \leq 4k_B T$), particularly for states lying within the right-handed funnel [Fig. 6(b)]. While this term accommodates the short helical segments that occur within the bulk of a helix or the fraying terminal regions associated with the canonical helix-coil transition, there is a dramatic overestimation of solvation penalties for centroids with low helical content. The introduction of an entropic term $\Delta G_C = \Delta E_T + \Delta E_O - T\Delta S_{\mathcal{R}}$ strengthens this correspondence [Fig. 6(c)] and may be rationalized as a form of energy–entropy compensation that corrects for the loss of inter-helical hydrogen bonds and helix dipole reinforcement. Nonetheless, notable deviations persist for a series of states lying within the low-energy regime, as well as within the large high entropy cluster consisting largely of unstructured configurations. REMD simulations indicate that a $p\Delta V$ term would shift the highest lying centroid energies by approximately $0.7 k_B T$ (see Fig. S12 of the [supplementary material](#)). However, the on-site and entropic terms already capture part of this correction due to the fitting. We thus neglect this correction.

It is natural to ask if these deviations are unique to a particular simulation temperature. To assess this possibility, an identical set of calculations was performed by transferring these parameters, and the full spin model [Eq. (4)], to four different environmental conditions (Fig. 7). A similar pattern of deviations between $\Delta G_{C,j}$ and ΔG_j is observed at each temperature, with a comparable quality of fit, suggesting a surprising degree of transferability for this model. The consistency of this behavior is highly suggestive of a systematic deviation between the spin model and all-atom simulations.

To dissect the origin of this behavior, it is helpful to examine a series of centroids that exhibit tight agreement with

replica exchange clusters. An ideal set is afforded by the right-handed helical funnel within the $T = 230$ K ensemble [Fig. 8(a)]. cursory analysis of these states reveals a classical helix-coil transition, proceeding from a well-formed α -helical

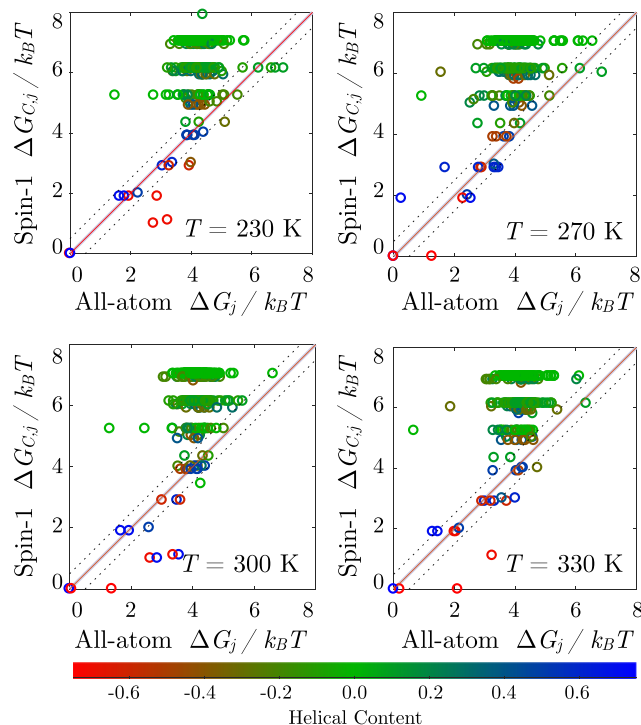


FIG. 7. Temperature dependence of cross correlation between the j -th cluster energy ΔG_j and the j -th centroid energy $\Delta G_{C,j}$ calculated using the full spin-1 model $\Delta G_C = \Delta E_T + \Delta E_O - T\Delta S$. Parameters are defined at each temperature so that $\hat{J}(R, R) = 1.0 k_B T$, $\hat{K}(U) = 0.9 k_B T$ and $s = 0.9$, following Fig. 6. Dashed lines denote the fitting range within $\pm 0.5 k_B T$ of the diagonal [overall RMSE_{230K} = $2.4 k_B T$; fit RMSE_{230K} = $0.3 k_B T$ (26 states); overall RMSE_{270K} = $2.6 k_B T$; fit RMSE_{270K} = $0.3 k_B T$ (19 states); overall RMSE_{300K} = $2.5 k_B T$; fit RMSE_{300K} = $0.3 k_B T$ (25 states); overall RMSE_{330K} = $2.4 k_B T$; fit RMSE_{330K} = $0.3 k_B T$ (19 states)].

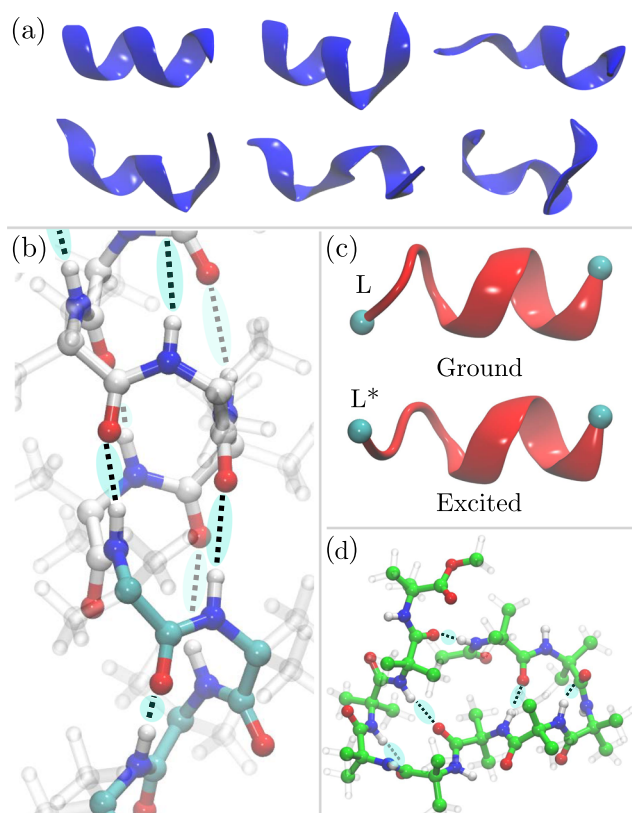


FIG. 8. Structural elements of the Aib₁₀ energy landscape: (a) selected centroids exhibiting tight cross correlation between the full spin model [Eq. (4)] and REMD simulations at $T = 230$ K, demonstrating a robust helix-coil transition; (b) cluster demonstrating both α - and 3_{10} -helical domains, shown in white (on top) and cyan (on bottom), respectively. Hydrogen bonding patterns are indicated by dotted lines and diffuse shading; (c) comparison between “ground” and “excited” state conformers sharing the same spin assignment; (d) anomalous cluster demonstrating an incommensurate hydrogen bonding pattern.

native state to a series of higher energy conformers characterized by fraying of the helix termini and the ultimate unwinding of the segment. The robust fit for this series is consistent with the enhanced stability of α -helical populations within Aib foldamers at low temperatures. Furthermore, the majority of these centroids retain a degree of helicity, suggesting that all but the highest-energy configurations in this series correspond to folds in which a helix has already nucleated.

It is notable that low energy clusters—exhibiting a reasonable correspondence between the spin-1 model and replica exchange simulations—are dominated by structures with substantial α -helical character (Fig. 3). Higher energy clusters are dominated by a 3_{10} -fold when nontrivial helicity is present. Manual inspection of poorly fit clusters reveals that many contain at least a small 3_{10} -helical twist, either in isolation (high-entropy cluster) or abutting an α -helical segment through a small unstructured linker (states below the diagonal). Owing to their distinct physical characteristics, these 3_{10} -helical folds constitute a distinct helical population that coexists alongside the dominant α -helical distribution [Fig. 8(b)]. A more physically accurate model might accommodate two distinct helical populations, forming a five-state representation. The prevalence of 3_{10} -helical configurations in short stretches

underscores a role as nucleation sites for α -helices, consistent with their purported role in macromolecular structure formation and with traditional analytical models for the helix-coil transition.^{64,65}

An additional family of deviations is associated with clusters that classify into the same spin encoding, yet differ conformationally within the REMD ensemble. These structures are generally related through a localized conformational distortion, which preserves the overall secondary structure yet places one conformer into a higher-energy configuration [Fig. 8(c)]. These energetically “excited” states were anticipated in earlier PCA analyses⁵⁹ and fall outside the scope of simple spin-based models (one needs further fine graining, i.e., a higher dimensional spin, to account for them), attesting to the importance of all-atom simulations for characterizing macromolecular energy landscapes. Underscoring this point, several of these configurations are highly populated (ΔG_j ranging between $2 k_B T$ and $3 k_B T$) and are associated with alterations in the terminal domains of the helix.

One final anomaly deserves further discussion. The atypical cluster located at $\Delta G_j \approx 1.5 k_B T$ and $\Delta G_{C,j} \approx 6 k_B T$ is accompanied by several similarly folded counterparts in both left and right helical funnels and deviates strongly from a helical fold while retaining a well-defined secondary structure [Fig. 8(d)]. These folds contain hydrogen bonding patterns consistent with single turns of 3_{10} - and α -helical character. Nonetheless, consecutive backbone hydrogen bonds from the i -th residue to residue $i + 3$ (3_{10} -helix) and from the i -th residue to residue $i + 4$ (α -helix) lie out of registry, and thus a long-distance helical structure fails to form. This behavior may be unique to the Aib₁₀ model, which exceeds the length of prior experimental constructs and lacks the bulky flanking groups present in synthetic helices. It is unlikely that this unconventional fold plays a role in the experimentally observed $L \leftrightarrow R$ interconversion due to constraints from the helix termini or the surrounding membrane environment. Nonetheless, simulations of the helix-coil transition in polyalanine indicate the presence of alternate folds that reside within shoulders of the folding funnel.⁹⁵ It is unclear if these clusters represent a similar behavior or if they correspond to a unique transition pathway between left-handed and right-handed funnels. While the latter possibility is less probable, it may only be excluded by mapping a kinetic network for these energy landscapes.

IV. CONCLUSIONS

Taken together, the observations herein underscore the complexity of seemingly simple macromolecular energy landscapes. From an analytical perspective, a three-state spin-1 model can accommodate the general structural motifs present within the conformational ensemble of Aib₁₀—corresponding to left-handed helices, right-handed helices, and unstructured coils. Nonetheless, the presence of competing α - and 3_{10} -helical subpopulations limits the scope of this approach. More complex five-state models can be constructed following Ising or Potts Hamiltonians; however, the presence of high-energy (“excited”) and low-energy (“ground”) conformational states with identical spin encodings suggests that

increasing the dimensions of the model will be met with diminishing returns. If a high resolution picture is required for the entire state spectrum, Markov state models⁹⁶ or transition path representations^{36–40} may afford a more efficacious—yet costly—approach.

Despite these limitations, the construction of simplified (and, in our case, analytical) models helps us to reveal key features of the energy landscape. These considerations extend to techniques for reduction of dimensionality—while PCA analysis reveals major minima, an approach based around replica exchange and unsupervised clustering captures states that might otherwise be masked when the resolution of simulation data is low. The importance of excited states and competing folds, as revealed through the spin-1 model, attests to the importance of careful landscape quantification. A judicious choice of methods is essential, balanced by a tradeoff between computational cost and resolution required of the resulting coarse-grained representation.

On a more sobering note, it is widely known that force-field dependence of the free energy landscape—and secondary structure, in particular—is a constant source of figurative, and sometimes literal, frustration.⁹⁷ For Aib, in particular, we find that α -helical content dominates at low energy (and 3_{10} at higher energy). The funnel crossover energetics are in agreement with other force fields, but the ratio of α to 3_{10} content for those cases is not available. Furthermore, experimental data and other MD simulations are not directly transferrable to the longer, unmodified, Aib polypeptide that we examine. Nevertheless, the inclusion of unstructured regions vastly improves coarse graining, irrespective of the force field—in this manner, we consider Aib₁₀ to be a model system for other helical macromolecules.^{15,22,41}

This gives a general lesson for coarse-graining, whether into discrete structural states or at the atomic scale: Full characterization of the energy landscape for protein fragments and polypeptides is possible. A comparison of structural features between all-atom, atomically coarse-grained, and discrete representations can therefore give a strong and quantitative assessment of what is physically occurring in these models—in our case, a $0.3 k_B T$ deviation of coarse grained states between $0 k_B T$ and $4 k_B T$ (this is in addition to constraints that ensure a correspondence with thermodynamic parameters and other data). In doing so, one can pinpoint deviations, determine symmetries and asymmetries, and, all-in-all, see what these complex atomic models are really yielding.

SUPPLEMENTARY MATERIAL

See [supplementary material](#) for a general evaluation of spin-1/2 and spin-1 model parameters.

ACKNOWLEDGMENTS

J.E.E. acknowledges support under the Cooperative Research Agreement between the University of Maryland and the National Institute for Standards and Technology Center for Nanoscale Science and Technology, Award No. 70NANB14H209, through the University of Maryland. K.A.V. was supported by the U.S. Department of Energy through

the LANL/LDRD Program. Computing resources were made available through the Los Alamos National Laboratory Institutional Computing Program, which is supported by the U.S. DOE National Nuclear Security Administration under Contract No. DE-AC52-06NA25396 as well as the Maryland Advanced Research Computing Center (MARCC).

APPENDIX: DEFINITION OF HELICAL ORDER PARAMETERS

Helical content is quantified^{98–100} using a function $\text{Hlx}\{\{\mathbf{x}_i\}\}$ that scores a given peptide configuration $\{\mathbf{x}_i\}$ based on (i) conformity to the angle formed by consecutive α -carbons in an ideal helix and (ii) consistency with an ideal hydrogen bonding arrangement for either an α -helix or a 3_{10} -helix,

$$\text{Hlx}\{\{\mathbf{x}_i\}\} = \frac{1}{2(N-2)} \sum_{i=1}^{N-2} \text{Ang}(\mathbf{x}_{\alpha,i}, \mathbf{x}_{\alpha,i+1}, \mathbf{x}_{\alpha,i+2}) + \frac{1}{2(N-m)} \sum_{i=1}^{N-m} \text{Hb}(\mathbf{x}_{\text{O},i}, \mathbf{x}_{\text{N},i+m}), \quad (\text{A1})$$

where $m = 3$ for a 3_{10} -helix, $m = 4$ for an α -helix, $\theta_0 = 90^\circ$ reflects the angle formed by three consecutive α -carbons, and $\Delta\theta_{\text{tol}} = 15^\circ$ defines an acceptance tolerance for deviations from an ideal helix. In this case, $\mathbf{x}_{\alpha,i}$, $\mathbf{x}_{\text{O},i}$, and $\mathbf{x}_{\text{N},i}$ denote, respectively, the α -carbon, amide oxygen, and amide nitrogen coordinates for the i -th residue. The angular deviation function $\text{Ang}(\mathbf{x}_{\alpha,i}, \mathbf{x}_{\alpha,i+1}, \mathbf{x}_{\alpha,i+2})$ is defined as

$$\text{Ang}(\mathbf{x}_{\alpha,i}, \mathbf{x}_{\alpha,i+1}, \mathbf{x}_{\alpha,i+2}) = \frac{1 - [\theta(\mathbf{x}_{\alpha,i}, \mathbf{x}_{\alpha,i+1}, \mathbf{x}_{\alpha,i+2}) - \theta_0]^2 / (\Delta\theta_{\text{tol}})^2}{1 - [\theta(\mathbf{x}_{\alpha,i}, \mathbf{x}_{\alpha,i+1}, \mathbf{x}_{\alpha,i+2}) - \theta_0]^4 / (\Delta\theta_{\text{tol}})^4}, \quad (\text{A2})$$

where $\theta(\mathbf{x}_{\alpha,i}, \mathbf{x}_{\alpha,i+1}, \mathbf{x}_{\alpha,i+2})$ is the angle formed by consecutive α -carbons and the hydrogen bonding contribution is quantified through

$$\text{Hb}(\mathbf{x}_{\text{O},i}, \mathbf{x}_{\text{N},i+R}) = \frac{1 - [|\mathbf{x}_{\text{O},i} - \mathbf{x}_{\text{N},i+R}|/d_0]^4}{1 - [|\mathbf{x}_{\text{O},i} - \mathbf{x}_{\text{N},i+R}|/d_0]^6}, \quad (\text{A3})$$

The orientation of a given peptide configuration $\{\mathbf{x}_i\}$ is assigned using the function

$$\text{Hcx}\{\{\mathbf{x}_i\}\} = \sum_{i=1}^{N-1} \text{hcx}\{\{\mathbf{x}_i\}, \{\mathbf{x}_{i+1}\}\}, \quad (\text{A4})$$

where the pairwise helical content is defined in terms of the (ϕ, ψ) dihedrals so that

$$\text{hcx}\{\{\mathbf{x}_i\}, \{\mathbf{x}_{i+1}\}\} = \begin{cases} 1 & (-100^\circ \leq \phi \leq -30^\circ; -80^\circ \leq \psi \leq -5^\circ) \\ 0 & \text{otherwise} \\ -1 & (100^\circ \geq \phi \geq 30^\circ; 80^\circ \geq \psi \geq 5^\circ) \end{cases} \quad (\text{A5})$$

reflects the net right-handed (positive) or left-handed helical content (negative), respectively.

¹M. Novotny and G. J. Kleywegt, *J. Mol. Biol.* **347**, 231 (2005).

²J. Venkatraman, S. C. Shankaramma, and P. Balam, *Chem. Rev.* **101**, 3131 (2001).

³R.-P. Hummel, C. Toniolo, and G. Jung, *Angew. Chem., Int. Ed.* **26**, 1150 (1987).

⁴D. J. Hill, M. J. Mio, R. B. Prince, T. Hughes, and J. S. Moore, *Chem. Rev.* **101**, 3893 (2001).

- ⁵T. A. Martinek and F. Fülöp, *Chem. Soc. Rev.* **41**, 687 (2012).
- ⁶B. A. F. Le Bailly and J. Clayden, *Chem. Commun.* **52**, 4852 (2016).
- ⁷M. De Poli, W. Zawodny, O. Quinero, M. Lorch, S. J. Webb, and J. Clayden, *Science* **352**, 575 (2016).
- ⁸R. Sakai, I. Otsuka, T. Satoh, R. Kakuchi, H. Kaga, and T. Kakushi, *Macromolecules* **39**, 4032 (2006).
- ⁹S. Li, K. Liu, G. Kuang, T. Masuda, and A. Zhang, *Macromolecules* **47**, 3288 (2014).
- ¹⁰J. E. Jones, V. Diemer, C. Adam, J. Raftery, R. E. Ruscoe, J. T. Sengel, M. I. Wallace, A. Bader, S. L. Cockcroft, J. Clayden, and S. J. Webb, *J. Am. Chem. Soc.* **138**, 688 (2015).
- ¹¹J. Suk, V. R. Naidu, X. Liu, M. S. Lah, and K.-S. Jeong, *J. Am. Chem. Soc.* **133**, 13938 (2011).
- ¹²M. Horeau, G. Lautrette, B. Wicher, B. Blot, J. Lebreton, M. Pipelier, D. Dubreuil, Y. Ferrand, and I. Huc, *Angew. Chem., Int. Ed.* **56**, 6823 (2017).
- ¹³J. Brioché, S. J. Pike, S. Tshepelevitsh, I. Leito, G. A. Morris, S. J. Webb, and J. Clayden, *J. Am. Chem. Soc.* **137**, 6680 (2015).
- ¹⁴F. G. A. Lister, B. A. F. Le Bailly, S. J. Webb, and J. Clayden, *Nat. Chem.* **9**, 420 (2017).
- ¹⁵M. Moradi, V. Babin, C. Roland, T. A. Darden, and C. Sagui, *Proc. Natl. Acad. Sci. U. S. A.* **106**, 20746 (2009).
- ¹⁶M. De Poli, M. De Zotti, J. Raftery, J. A. Aguilar, G. A. Morris, and J. Clayden, *J. Org. Chem.* **78**, 2248 (2013).
- ¹⁷C. M. Goodman, S. Choi, S. Shandler, and W. F. DeGrado, *Nat. Chem. Biol.* **3**, 252 (2007).
- ¹⁸J. D. Bryngelson and P. G. Wolynes, *Proc. Natl. Acad. Sci. U. S. A.* **84**, 7524 (1987).
- ¹⁹J. D. Bryngelson and P. G. Wolynes, *J. Phys. Chem.* **93**, 6902 (1989).
- ²⁰P. E. Leopold, M. Montal, and J. N. Onuchic, *Proc. Natl. Acad. Sci. U. S. A.* **89**, 8721 (1992).
- ²¹K. Röder and D. J. Wales, "Evolved minimal frustration in multifunctional biomolecules," *J. Phys. Chem. B* (published online 2018).
- ²²D. Chakrabarti and D. J. Wales, *Soft Matter* **7**, 2325 (2011).
- ²³S. W. Olesen, S. N. Fejer, D. Chakrabarti, and D. J. Wales, *RSC Adv.* **3**, 12905 (2013).
- ²⁴D. J. Wales, M. A. Miller, and T. R. Walsh, *Nature* **394**, 758 (1998).
- ²⁵J. P. K. Doye, M. A. Miller, and D. J. Wales, *J. Chem. Phys.* **110**, 6896 (1999).
- ²⁶F. Calvo, J. P. Neirrotti, D. L. Freeman, and J. D. Doll, *J. Chem. Phys.* **112**, 10350 (2000).
- ²⁷J. P. Neirrotti, F. Calvo, D. L. Freeman, and J. D. Doll, *J. Chem. Phys.* **112**, 10340 (2000).
- ²⁸V. A. Mandelshtam, P. Frantsuzov, and F. Calvo, *J. Phys. Chem. A* **110**, 5326 (2006).
- ²⁹D. J. Wales and T. V. Bogdan, *J. Phys. Chem. B* **110**, 20765 (2006).
- ³⁰V. A. Sharapov, D. Meluzzi, and V. A. Mandelshtam, *Phys. Rev. Lett.* **98**, 105701 (2007).
- ³¹F. Calvo, *Phys. Rev. E* **82**, 046703 (2010).
- ³²D. J. Wales, *Chem. Phys. Lett.* **584**, 1 (2013).
- ³³R. M. Seghal, D. Maroudas, and D. M. Ford, *J. Chem. Phys.* **140**, 104312 (2014).
- ³⁴D. J. Wales, *J. Chem. Phys.* **142**, 130901 (2015).
- ³⁵M. T. Oakley, R. L. Johnston, and D. J. Wales, *Phys. Chem. Chem. Phys.* **15**, 3965 (2013).
- ³⁶D. J. Wales, *Mol. Phys.* **100**, 3285 (2002).
- ³⁷D. J. Wales, *Mol. Phys.* **102**, 891 (2004).
- ³⁸G. Adjanor, M. Athènes, and F. Calvo, *Eur. Phys. J. B* **53**, 47 (2006).
- ³⁹M. Picciani, M. Athènes, J. Kurchan, and J. Tailleur, *J. Chem. Phys.* **135**, 034108 (2011).
- ⁴⁰M. Cameron and E. Vanden-Eijnden, *J. Stat. Phys.* **156**, 427 (2014).
- ⁴¹D. Chakraborty and D. J. Wales, *Phys. Chem. Chem. Phys.* **19**, 878 (2017).
- ⁴²M. Kouza and U. H. E. Hansmann, *J. Phys. Chem. B* **116**, 6645 (2012).
- ⁴³K. Röder and D. J. Wales, *J. Chem. Theory Comput.* **13**, 1468 (2017).
- ⁴⁴D. Chakraborty and D. J. Wales, *J. Phys. Chem. Lett.* **9**, 229 (2018).
- ⁴⁵A. J. Doig, in *Protein Folding, Misfolding, and Aggregation: Classical Themes and Novel Approaches*, edited by V. Munoz (Royal Society of Chemistry, 2008).
- ⁴⁶Y. Paterson, S. Rumsey, E. Benedetti, G. Némethy, and H. A. Scheraga, *J. Am. Chem. Soc.* **103**, 2947 (1981).
- ⁴⁷L. Zhang and J. Hermans, *J. Am. Chem. Soc.* **116**, 11915 (1994).
- ⁴⁸R. Bürge, X. Daura, M. Bellanda, S. Mammi, E. Peggion, and W. van Gunsteren, *J. Pept. Res.* **57**, 107 (2001).
- ⁴⁹R. Improta, V. Barone, K. N. Kudin, and G. E. Scuseria, *J. Am. Chem. Soc.* **123**, 3311 (2001).
- ⁵⁰J. Mahadevan, K.-H. Lee, and K. Kuczera, *J. Phys. Chem. B* **105**, 1863 (2001).
- ⁵¹R. Schweitzer-Stenner, W. Gonzales, G. T. Bourne, J. A. Feng, and G. R. Marshall, *J. Am. Chem. Soc.* **129**, 13095 (2007).
- ⁵²S. Grubišić, G. Brancato, and V. Barone, *Phys. Chem. Chem. Phys.* **15**, 17395 (2013).
- ⁵³S. Grubišić, B. Chandramouli, V. Barone, and G. Brancato, *Phys. Chem. Chem. Phys.* **18**, 20389 (2016).
- ⁵⁴V. Botan, E. H. G. Backus, R. Pfister, A. Moretto, M. Crisma, C. Toniolo, P. H. Nguyen, G. Stock, and P. Hamm, *Proc. Natl. Acad. Sci. U. S. A.* **104**, 12749 (2007).
- ⁵⁵E. H. G. Backus, P. H. Nguyen, V. Botan, R. Pfister, A. Moretto, M. Crisma, C. Toniolo, G. Stock, and P. Hamm, *J. Phys. Chem. B* **112**, 9091 (2008).
- ⁵⁶E. H. G. Backus, P. H. Nguyen, V. Botan, A. Moretto, M. Crisma, C. Toniolo, O. Zerbe, G. Stock, and P. Hamm, *J. Phys. Chem. B* **112**, 15487 (2008).
- ⁵⁷M. Schade, A. Moretto, M. Crisma, C. Toniolo, and P. Hamm, *J. Phys. Chem. B* **113**, 13393 (2009).
- ⁵⁸P. H. Nguyen, S.-M. Park, and G. Stock, *J. Chem. Phys.* **132**, 025102 (2010).
- ⁵⁹S. Buchenberg, N. Schaudinnus, and G. Stock, *J. Chem. Theory Comput.* **11**, 1330 (2015).
- ⁶⁰F. Sittel, T. Filk, and G. Stock, *J. Chem. Phys.* **147**, 244101 (2017).
- ⁶¹H. S. Chan and K. A. Dill, *J. Chem. Phys.* **99**, 2116 (1993).
- ⁶²H. S. Chan and K. A. Dill, *J. Chem. Phys.* **100**, 9238 (1994).
- ⁶³J. P. K. Doye and D. J. Wales, *J. Chem. Phys.* **111**, 11070 (1999).
- ⁶⁴B. H. Zimm and J. K. Bragg, *J. Chem. Phys.* **31**, 526 (1959).
- ⁶⁵S. Lifson and A. Roig, *J. Chem. Phys.* **34**, 1963 (1961).
- ⁶⁶M. S. Shapovalov and R. L. Dunbrack, *Structure* **19**, 844 (2011).
- ⁶⁷L. Martínez, R. Andrade, E. G. Bergin, and J. L. Martínez, *J. Comput. Chem.* **30**, 2157 (2009).
- ⁶⁸R. B. Best, X. Zhu, J. Shim, P. E. M. Lopes, J. Mittal, M. Feig, and A. D. MacKerell, Jr., *J. Chem. Theory Comput.* **8**, 3257 (2012).
- ⁶⁹S. Plimpton, *J. Comput. Phys.* **117**, 1 (1995).
- ⁷⁰A. D. MacKerell, Jr., M. Feig, and C. L. Brooks III, *J. Am. Chem. Soc.* **126**, 698 (2004).
- ⁷¹D. I. Freedberg, R. M. Venable, A. Rossi, T. E. Bull, and R. W. Pastor, *J. Am. Chem. Soc.* **126**, 10478 (2004).
- ⁷²K. K. Patapati and N. M. Glykos, *Biophys. J.* **101**, 1766 (2011).
- ⁷³W. Shinoda, M. Shiga, and M. Mikami, *Phys. Rev. B* **69**, 134103 (2004).
- ⁷⁴G. J. Martyna, D. J. Tobias, and M. L. Klein, *J. Chem. Phys.* **101**, 4177 (1994).
- ⁷⁵M. Parrinello and A. Rahman, *J. Appl. Phys.* **52**, 7182 (1981).
- ⁷⁶T. Okabe, M. Kawata, Y. Okamoto, and M. Masuhiro, *Chem. Phys. Lett.* **335**, 435 (2001).
- ⁷⁷Y. Mori and Y. Okamoto, *J. Phys. Soc. Jpn.* **79**, 074003 (2010).
- ⁷⁸E. H. G. Backus, R. Bloem, R. Pfister, A. Moretto, M. Crisma, C. Toniolo, and P. Hamm, *J. Phys. Chem. B* **113**, 13405 (2009).
- ⁷⁹M. Kobus, P. H. Nguyen, and G. Stock, *J. Chem. Phys.* **133**, 034512 (2010).
- ⁸⁰M. Kobus, P. H. Nguyen, and G. Stock, *J. Chem. Phys.* **134**, 124518 (2011).
- ⁸¹A. K. Francis, M. Iqbal, P. Balaram, and M. Vijayan, *FEBS Lett.* **155**, 230 (1983).
- ⁸²A. Bavoso, E. Benedetti, B. Di Blasio, V. Pavone, C. Pedone, C. Toniolo, and G. M. Bonora, *Proc. Natl. Acad. Sci. U. S. A.* **83**, 1988 (1986).
- ⁸³R. Gessmann, H. Brückner, and K. Petratos, *J. Pept. Sci.* **9**, 753 (2003).
- ⁸⁴S. C. Yasui, T. A. Keiderling, F. Formaggio, G. M. Bonora, and C. Toniolo, *J. Am. Chem. Soc.* **108**, 4988 (1986).
- ⁸⁵S. C. Yasui, T. A. Keiderling, G. M. Bonora, and C. Toniolo, *Biopolymers* **25**, 79 (1986).
- ⁸⁶H. Maekawa, F. Formaggio, C. Toniolo, and N.-H. Ge, *J. Am. Chem. Soc.* **130**, 6556 (2009).
- ⁸⁷M. Bellanda, E. Peggion, S. Mammi, R. Bürge, and W. van Gunsteren, *J. Pept. Res.* **57**, 97 (2001).
- ⁸⁸D. J. Kuster, C. Liu, Z. Fang, J. W. Ponder, and G. R. Marshall, *PLoS One* **10**, e0123146 (2015).
- ⁸⁹J. R. Gord, D. M. Hewett, A. O. Hernandez-Castillo, K. N. Blodgett, M. C. Rotondaro, A. Varuolo, M. A. Kubasik, and T. S. Zwier, *Phys. Chem. Chem. Phys.* **18**, 25512 (2016).

- ⁹⁰S. Carlotto, P. Cimino, M. Zerbetto, L. Franco, C. Corvaja, M. Crisma, F. Formaggio, C. Toniolo, A. Polimeno, and V. Barone, *J. Am. Chem. Soc.* **129**, 11248 (2007).
- ⁹¹I. A. Topol, S. K. Burt, E. Derety, T.-H. Tang, A. Perczel, A. Rashin, and I. G. Csizmadia, *J. Am. Chem. Soc.* **123**, 6054 (2001).
- ⁹²S. V. Krivov and M. Karplus, *Proc. Natl. Acad. Sci. U. S. A.* **101**, 14766 (2004).
- ⁹³S. V. Krivov and M. Karplus, *J. Phys. Chem. B* **110**, 12689 (2006).
- ⁹⁴R. B. Best and G. Hummer, *Proc. Natl. Acad. Sci. U. S. A.* **107**, 1088 (2010).
- ⁹⁵Y. Levy, J. Jortner, and O. M. Becker, *Proc. Natl. Acad. Sci. U. S. A.* **98**, 2188 (2001).
- ⁹⁶F. Noé and S. Fischer, *Curr. Opin. Struct. Biol.* **18**, 154 (2008).
- ⁹⁷P. L. Freddolino, S. Park, B. Roux, and K. Schulten, *Biophys. J.* **96**, 3772 (2009).
- ⁹⁸M. Iannuzzi, A. Laio, and M. Parrinello, *Phys. Rev. Lett.* **90**, 238302 (2003).
- ⁹⁹D. Alemari, F. Collu, M. Cascella, and M. Dal Peraro, *J. Chem. Theory Comput.* **6**, 315 (2010).
- ¹⁰⁰G. Fiorin, M. L. Klein, and J. Hénin, *Mol. Phys.* **111**, 3345 (2013).